Northward Channel flow in Northern Tibet revealed from 3D magnetotelluric modelling

Wenbo Wei[a], Florian Le Pape[b], Alan G. Jones[b], Jan Vozar[b], Hao Dong[a], Martyn J. Unsworth[c], Sheng Jin[a], Gaofeng Ye[a], Jianen Jing[a], Letian Zhang[a] and Chengliang Xie[a]

[a]*China University of Geosciences Beijing, 29 Xueyuan Road, Beijing, 100083, China*
[b]*Dublin Institute for Advanced Studies, 5 Merrion Square, Dublin 2, Ireland* [c]*Department of Physics, University of Alberta, Edmonton, AB, T6G 2J1, Canada*

Abstract

The Kunlun fault defines one of the major northern tectonic boundaries of the Tibetan plateau. Previous geophysical studies have detected a major change in rheology across this boundary, but it is not clear how this is related to models that have invoked crustal flow. The lithospheric resistivity structure of the Kunlun Fault has been investigated by both the INDEPTH III and IV magnetotelluric (MT) transects. All the MT data were processed using modern statistically-robust methods, and have been analysed for directionality and dimensionality. In order to improve understanding of the anisotropic distribution of melt previously revealed by our remodelling of the INDEPTH III MT data, a variant approach on 3D inversion of 2D profiles was investigated to explore and improve lateral resolution. In addition to the apparent surficial deformation associated with the sinistral strike-slip Kunlun fault, the 3D modelling of the INDEPTH MT data reveals that complex deformation processes are occurring at mid-crustal depths in northern Tibet. The 3D MT inversion results, supported by synthetic modelling, particularly confirm and highlight the presence of separate north-south intrusions of conductive material crossing the Kunlun fault into the more resistive Kunlun-Qaidam block. These north-south intrusions are interpreted to be associated with the horizontal channel flow of partially molten Songpan-Ganzi crust into two (or more) separated channels moving northwards and crossing the surficial trace of the Kunlun fault at mid-to-lower crustal depths.

1. Introduction

The first INDEPTH (InterNational DEep Profiling of Tibet and the Himalaya) experiments in the early to mid-1990s collected seismic and magnetotelluric data that revealed the presence of a partially molten middle crust beneath southern Tibet (Nelson et al., 1996, and papers in that special issue). The revolutionary interpretation of those data by Nelson et al. (1996) instigated a whole new insight into crustal processes during continent-continent collision and has led to geodynamicists, geologists and tectonicists examining the concept of "channel flow". The Himalayan channel flow model (e.g., Beaumont et al., 2001) was directly built from those results in order to explain the high-grade metamorphic rocks, leucogranites and migmatites exposed in the Greater Himalayan sequence (Godin et al., 2006), with the INDEPTH-II 1995 magnetotelluric results being key to the development of the observation of partial melt in the crust (Chen et al., 1996).

Furthermore, in order to account for the overall deformation observed in the whole of the Tibetan Plateau, a range of geodynamic models have been proposed, the most popular of them being the crustal flow model of Royden (Royden et al., 1997; Clark and Royden, 2000). This type of deformation is dominated by rapid ductile flow in the middle and/or lower crust (e.g., Klemperer, 2006). The crustal flow has been proposed to escape to the east, moving around the eastern Himalayan syntaxis and being blocked by the rigid Sichuan basin (Clark and Royden, 2000). However, in contrast to the observations along the Himalaya, there is no direct geological evidence for crustal flow beneath the eastern margin of the Tibetan Plateau, as the Longmenshan ranges do not show either horizontal extrusion of deep crustal metamorphic rocks or equivalents to the Main Central Thrust (MCT) or South Tibetan Detachment (STD) (Searle et al., 2011). Harris (2007) proposed that "channel

63   tunnelling" (Beaumont et al., 2001) could be occurring in eastern Tibet, as the weak

64   crustal layer may not reach the surface. Medvedev and Beaumont (2006) suggested

65   the channel flow model as a mechanism to characterize the progressive growth of the

66   Tibetan plateau.

67   In central Tibet, the absence of seismic evidence for earlier accretion in the

68   deep crust has been related to lateral escape by ductile flow (Haines et al., 2003). This

69   observation was also recently supported by the widespread low velocities in the

70   middle-to-lower crust of northern Tibet imaged from ambient-noise tomography

71   (Karplus et al., 2013). Magnetotelluric (MT) studies have significantly contributed to

72   the characterization of the Tibetan crustal flow (Chen et al., 1996; Li et al., 2003;

73   Unsworth et al., 2004; Rippe and Unsworth, 2010; Bai et al., 2010; Le Pape et al.,

74   2012). MT studies highlighted the presence of two laterally-extensive mid-crustal

75   conductors that were interpreted as channels of crustal flow or shear zones on the

76   margins of a region of extruding crust extending from the Tibetan plateau into

77   southwest China and covering a horizontal distance of more than 800 km (Bai et al.,

78   2010). Low shear-wave velocities imaged from surface-wave tomography in

79   southeastern Tibet show spatial variations in the strength of the middle and lower

80   crust (Yao et al., 2008). Thus, Bai et al. (2010) and Yao et al. (2008) are in agreement

81   that the inferred crustal flow in Tibet may characterize a pattern of deformation more

82   complex than the previously established model of Clark and Royden (2000).

83   INDEPTH Phase IV was initiated with its overarching goal to develop a

84   better understanding of the structure and evolution of the northern margins of the

85   Tibetan plateau defined by the Kunlun and Altyn Tagh faults. In particular, seismic

86   results from INDEPTH IV have highlighted the possible flow of the weaker and more

87   easily deformable Songpan-Ganzi crust into the crust beneath the Qaidam basin

88   (Karplus et al., 2011; Mechie et al., 2012). This interpretation is also supported by the

89   2D anisotropic re-modelling of the INDEPTH III MT data that inferred that partial

90   melt was intruding across the Kunlun fault in a finger-like manner (Le Pape et al.,

91   2012). However, the study of Le Pape et al. (2012) was not able to establish definite

92   constraints on the geometries of the melt intrusions. In order to investigate further the

93   pattern of melt distribution within the crust beneath the Kunlun Fault, the new MT

94   data from the INDEPTH phase IV campaign was combined with the northernmost

95   stations of the INDEPTH III 600-line profile, previously interpreted by Unsworth et

96   al. (2004) and Le Pape et al. (2012), to obtain a 3D resistivity model of the Kunlun

97   region. Due to the limitations of station coverage, the array was not ideal for a 3D

98   inversion. Thus a novel approach was developed for the 3D inversion of MT data

99   located on 2D profiles. This investigated ways to improve the lateral resolution by

100 limiting the introduction of off-profile artefacts.

101
102
103 **2. Geological setting**
104
105   2.1. **Songpan-Ganzi terrane**
106
107   The Songpan-Ganzi terrane is bounded to the north by the Kunlun Fault

108 (KF), a reactivation of the older Anyimagen-Kunlun-Muztagh suture that separates

109 the terrane from the Kunlun-Qaidam block (Fig. 1). To the south, the Songpan-Ganzi

110 terrane is separated from the Qiangtang terrane by the Jinsha Suture (JRS, Fig. 1).

111 The terrane consists mostly of Upper Triassic marine strata characterized by a thick

112 sequence of turbidites, also named the Songpan-Ganzi flysch complex, that are

113 several kilometres in thickness lying on top of Palaeozoic marine sediments

114 belonging to the passive margin of north China (Yin and Harrison, 2000; Gehrels et

115 al., 2011). The Songpan-Ganzi flysch complex underwent intense folding and

116 thrusting during the Triassic collision between the North and South China blocks

117 (Burchfiel et al., 1995; Yin and Nie, 1996), forming the Anyimagen-Kunlun-Muztagh

118 suture. East of the Lhasa-Golmud highway in the north of the terrane, the Bayan Har

119 Shan defines the southern branch of the Kunlun Shan. The Bayan Har mountains are

120 characterized by poorly dated low-grade slate belts, which include Triassic

sedimentary rocks and Mesozoic plutonic intrusions (Cowgill et al., 2003; Huang et al., 2004).

2.2. **Kunlun-Qaidam terrane**

The Eastern Kunlun-Qaidam Terrane lies between the Anyimaqen-Kunlun-Muztagh suture to the south and the Qilian suture to the north (Yin and Harrison, 2000). The terrane is bounded in the south by the Kunlun mountains, or Kunlun Shan, along the active sinistral Kunlun fault. Near the Lhasa-Goldmud highway (Fig. 1), the fault splits in two branches, characterizing the Kunlun Fault (KF) and the South Kunlun Fault (SKF) (Fig. 1). Different interpretations have been offered concerning the structure of the Kunlun fault at depth. Kirby et al. (2007) proposed that it terminates within the thickened crust of the Tibetan plateau, whereas Meyer et al. (1998) suggested the fault to be a lithospheric discontinuity that extends as deep as 150 km (Tapponier et al., 2001). More recently, the seismic results of Karplus et al. (2011, 2013) indicated that the fault may not extend deeper than 30 km, i.e., the middle of the overly-thickened Tibetan crust. The Kunlun fault is likely to be coeval with the Miocene extension and links the eastward expansion of the Tibetan plateau with the north-south trending extensional systems (Yin and Harrison, 2000). The Kunlun Shan exhibit mainly Paleozoic and lower Mesozoic rocks intruded by early Paleozoic and Permo-Triassic arc-type magmatism, characterized as the Kunlun batholith (Yin and Harrison, 2000). The Qaidam basin is bounded by the Kunlun Shan in the south, the Altan Shan in the northwest and the Qilian Shan-Nan Shan in the northeast (Fig. 1 inset). As fold and thrust belts developed along the foreland of the Kunlun Shan mountain belt, the Qaidam basin expanded progressively toward the north and east (Yin et al., 2008). The southeast-dipping North Kunlun Thrust (NKT) appends Proterozoic metamorphic rocks and Paleozoic sedimentary and igneous rocks over the Tertiary and Cenozoic strata of the Qaidam crust (Yin and Harrison, 2000).

3. MT data analysis

The INDEPTH IV MT data were acquired between late Spring and early Summer 2010 and define the 6000 profile. Originally, it was planned for them to be acquired in 2009, but the very low sunspot activity at the tail of Solar Cycle 23 precluded acquisition. As depicted on Fig. 1, the new MT 6000 profile (sites denoted by purple squares) is located to the east of the previously collected INDEPTH III 600-line (sites denoted by black squares) and extends from the middle of the Songpan-Ganzi terrane, in the western Bayan Har Shan, to the southern edge of the Qaidam basin. The INDEPTH III 600 and INDEPTH IV 6000 profiles become closely aligned in the Qaidam basin as they meet up south of the north Kunlun thrust (NKT) on the only road crossing the Kunlun range (Fig. 1). The new 6000 MT transect was also purposely collocated with the INDEPTH IV seismic profile (Karplus et al., 2011; Mechie et al., 2012).

For this 3D study, MT data from a total of 38 sites from both INDEPTH III and IV transects were selected, mainly from the Kunlun fault area (Fig. 1). The data include 14 sites from the INDEPTH III 600-line and 24 sites from the new INDEPTH IV 6000-line. Overall, the data comprise 10 long period MT (LMT) sites merged with broadband (BBMT) data sites from each profile, the remaining 18 sites only having BBMT data. For the INDEPTH IV sites, all the LMT data were processed using the processing method of Smirnov (2003). The BBMT data were processed using the commercial code from Phoenix Geophysics which is based on the algorithm of Jones and Jödicke (1984, method 6 in Jones et al., 1989), which uses a method called in the statistical literature Least Trimmed Squares developed independently at the same time as Jones and Jödicke (1984) by Rousseeuw (1984). Both the LMT and the BBMT data were processed using remote reference data to reduce the effects of noise contributions on the MT impedance tensor estimates. As mentioned in Le Pape et al. (2012), the INDEPTH III time series data were processed with the codes from Egbert

181 (1997) and Jones et al. (1989) using remote reference data when available. For both

182 INDEPTH III and IV, the BBMT and LMT data were merged at common locations.

183   Prior to inversion, the dimensionality of the data and the distribution of

184 regional conductive structures were investigated qualitatively through phase tensor

185 and induction vector analysis for different period bands (Fig. 2). The main advantage

186 of these tools is that they are independent of the electric effects of galvanic distortion

187 (but not the magnetic effects) (Jones, 2012). The real induction arrows are plotted in

188 the Parkinson's convention (Parkinson, 1959), meaning that they are reversed so that

189 they will point towards conductive anomalies (Jones, 1986) (in contrast to the Weise

190 convention, where the arrows points away from conductors). Not all sites showed

191 good quality tipper data, therefore only induction arrows from selected sites have

192 been introduced on Figure 2. The phase tensor ellipses are plotted with the skew

193 angle. The skew angle measures the asymmetry in the MT response and therefore

194 large values of skew angle can be linked to the presence of 3D regional conductive

195 structures (Caldwell et al., 2004). With values outside the [-3° 3°] interval, it can be

196 considered that the data is exceeding the limits of quasi 2D approximations.

197 Furthermore, the direction of the phase tensor major axis will usually align with the

198 direction of the maximum inductive current flow (Caldwell et al., 2004). However,

199 since the induction arrows and phase tensor do not sample the same volume they

200 cannot be always comparable. Only period longer than 100 s were investigated to

201 focus mainly on the regional structures but also because at the shorter periods the

202 induction vectors were relatively scattered. On Fig. 2, both phase tensor and induction

203 vector parameters have been averaged to an error-weighted mean over each period

204 interval. Over most period intervals, both phase tensor ellipses and induction vectors

205 calculated from the INDEPTH data show a strong consistency between neighbouring

206 sites and periods.

207   To the north, the effects of the high conductivity of the Qaidam basin, that is

208 related to extensive salt deposits (Kezao and Bowler, 1986), are seen on the northern

209 most stations. The induction vectors sense the high conductivity basin by pointing to

210 the north, at periods < 800 s. It is also worth noting that the low resistivity layer in the

211 Qaidam Basin limits the depth of penetration of the MT signals, due to the strong

212 screening effects of the conducting layer. At most sites located south of the SKF,

213 there is an overall east-west trend in the orientation of the ellipses, in agreement with

214 the directions of the main geological sutures in the study area. Between the SKF and

215 the NKT, the real induction vectors, although not strong, point west, indicating a

216 region of more complex 3D structure. This 3D signature is confirmed by the high

217 skew values observed in the Kunlun area. Those high values are likely associated

218 with small- to middle-scale 3D structures located beneath the Kunlun mountains.

219

220

221 ## 4. 3D modelling of MT data from Northern Tibet

222

223 In this section we present the 3D inversion models derived from the

224 INDEPTH III and IV MT data in association with a 3D inversion of synthetic MT

225 data that explored the limitations in lateral resolution caused by the restricted grid of

226 MT stations. The algorithm used for the 3D inversions was WSINV3DMT, which is

227 based on data space inversion method and developed from the OCCAM minimum-

228 norm approach (Siripunvaraporn et al., 2005a). Furthermore, it is worth noting that,

229 due to the sparse stations layout, 3D inversion applied on 2D profiles should include

230 all elements of the impedance tensor to improve off-profile resolution of nearby

231 structures, as highlighted in Siripunvaraporn et al. (2005b) and Kiyan et al. (2014).

232 Therefore, in the following 3D inversions of real and synthetic MT data, the full

233 impedance tensor responses were inverted. In this study the objective was to

234 primarily focus on the comparison in lateral resolution from different approaches of

235 3D modelling of both real and synthetic data impedances. For this reason and due to

236 the poor quality of the tipper data for a few sites, no tipper data were introduced in

237 the modelling. For each model, the misfit was reduced by running a few successive

238 inversions using each resulting model as the starting and *a priori* model for the next

239 inversions. The size of the 3D mesh used for the inversion of INDEPTH data was 80

240 x 75 x 44 cells with a 5 x 5 km horizontal gridding in a square zone defined by the

241 stations locations. For the synthetic modelling, the size of the 3D mesh used was

242 60x61x48 cells with also a 5 x 5 km horizontal gridding around the stations.

243
244
245

246 ## 4.1. **3D Inversion of the INDEPTH III and IV data**

247

248 The starting model and *a priori* model for the initial inversion was a 100

249 Ω.m layer located above a fixed 10 Ω.m halfspace (i.e., locked during inversion) at

250 410 km that represented the mantle transition zone. This deep basal conductor is

251 required in all 2D and 3D modelling of MT data to ensure that the boundary condition

252 on the base of the model is satisfied and to prevent bleeding down of features as a

253 consequence of the spatial regularization. An error floor of 5% of the geometrically-

254 averaged off-diagonal impedances was used to set a minimum error bar of $0.05 * (Z_{xy}$

255 $* Z_{yx})^2$ applied on all four elements of the impedance tensor during the inversion.

256 Periods in the range 0.003 to 10000 s were used and uniformly distributed with 4

257 periods per decade. The final 3D inversion model is plotted in Fig. 3 as several

258 horizontal slices and vertical cross-sections. The 3D inversion of the 38 MT sites

259 selected from both INDEPTH III and IV profiles, gave an overall RMS (Root Mean

260 Square) misfit of 2.3. Furthermore, the misfit at each site describes a relatively

261 homogeneous error partitioning across each station, although two sites in the Kunlun

262 Shan area show high RMS misfit values (Fig. 3). As seen in Fig. 4, the overall

263 observed and calculated responses are very similar, except for some localized

264 exceptions. For instance, one of the most striking differences between the observed

265 and calculated data occurs at the shortest periods of INDEPTH IV data in the XX and

266 YY components. For those components, both the apparent resistivity and phase

267 exhibit 3D signatures in the observed responses whereas the calculated responses

268 appear more 1D. This difference is mainly due to the size of the mesh used in the

269   inversion, which was limited by computational restrictions.

270   Shallower crustal features can be clearly seen on the horizontal slice at 5 km.
271   The trace of the NKT is unmistakably highlighted by the transition between the more
272   resistive terrane of the Kunlun ranges and the more conductive sediments of the
273   Qaidam basin to the north. The traces of both the KF and the SKF are also quite
274   coherent with the surrounding resistivity distribution, particularly at the level of the
275   600-line. To the south, conductive structure "A" following the 600-line profile is
276   electrical evidence of the sediments of the Songpan-Ganzi terrane, including the
277   widespread Triassic flysch deposits. Finally, the main resistive features observed at 5
278   km depth on the 3D model correlate relatively well with the resistive crust "B" of the
279   Kunlun Shan in the north and the resistive crust "C" of the western Bayan Har
280   mountains to the east at the southern end of the INDEPTH IV profile (Fig. 3). Down
281   to 20 km, the plan view shows a widespread conductive anomaly to the south of the
282   INDEPTH III profile, whereas south of the INDEPTH IV line there is a strong
283   alternation between conductive and resistive structures "D", likely related to the more
284   complex crustal structure of the Bayan Har mountains. Further north, the resistive
285   root "B" of the Kunlun mountains can also be seen, but a conductive anomaly "E" is
286   located where both profiles meet between the surficial traces of the KF and the NKT.
287   When reaching the 37 and 55 km depth views of the 3D model, the 600 and 6000
288   lines show a significant conductive anomaly "F" south of the SKF. Although less
289   conductive, the anomaly "F" extends further north across the KF. Meanwhile, the
290   conductive feature "E" observed at 20 km south of the NKT migrates further east of
291   the 6000 line.

292   Both cross-sections, labelled 2 and 3 in Fig. 3, show that the mid-crustal
293   conductor "F" located beneath the Songpan-Ganzi terrane weakens further to the
294   north as it extends beneath the Kunlun fault system (Fig. 3). Furthermore, on a more
295   global scale they also reveal the clear separation between the Tibetan conductive
296   crust to the south and a more resistive lithosphere to the north beneath the Kunlun-

297   Qaidam block. A smeared conductive layer "G" characterizing the Qaidam basin can

298   also be seen on cross section 3. Although mainly located outside of the profile and

299   therefore poorly constrained, cross-section 1 (Fig. 3) was chosen to highlight the

300   presence of the conductive structure "H" located in the upper mantle north of the

301   Kunlun fault. This conductive anomaly can also be seen on the 37 and 55 km plan

302   views as well as at the northern edge of cross-section 2 as it becomes shallower

303   towards the east. This anomaly "H" is likely to be an inversion artefact that reflects

304   the lack of lateral resolution in the inversion, due to the paucity of data controlling it,

305   and therefore must be treated with caution.

306   These inversion results, although 3D, are derived from two relatively linear

307   profiles which raises questions about the limits of lateral resolution and the spreading

308   of anomalies as an artefact of the smoothness regularization. In order to test for

309   resolution and obtain a better understanding of the limits of a one-profile 3D

310   inversion, some of the 3D synthetic models for northern Tibet, already discussed in

311   Le Pape et al. (2012) are re-considered for the 3D inversion of a synthetic profile

312   below.

313
314
315   ## 4.2. Synthetic modelling and inversions
316
317   Although the inversion model presented above is fully 3D, it must be

318   appreciated that it is mainly the result of the inversion of MT data on two sub-parallel

319   profiles. The apparent lack of station coverage, in contrast to an ideal layout of

320   stations in a grid manner, raises questions about the limit of lateral resolution in the

321   3D model. However, as presented by Siripunvaraporn et al. (2005b), 3D inversion of

322   a 2D profile can significantly improve the interpretation of structures located

323   underneath and, significantly, around the profile. Here, two particular models A and

324   B, shown in Fig. 5, were investigated for 3D resolution. For consistency, they are

325   based on the 3D synthetic models already presented in Le Pape et al. (2012). Both

326   models were generated to account for melt intrusions defining the 3D resistivity

327 transition between the Songpan-Ganzi and the more resistive eastern Kunlun-Qaidam

328 block to the north observed in the recent 2D anisotropic MT model of the 600-line.

329 The models describe similar geometries and only differ through the orientation of the

330 intrusions. This synthetic study particularly aims at exploring and discovering how

331 those synthetic intrusions and their associated orientations can be recovered and

332 interpreted from 3D inversions. The 3D synthetic data were generated using the 3D

333 forward code in WinGLink of Mackie et al. (1994). Furthermore, 2.5% random noise

334 was added to the numerically calculated impedances of the 19 stations per profile.

335 As for the real MT data, the 3D inversion code WSINV3DMT

336 (Siripunvaraporn et al., 2005a) was used to invert the full impedance tensors from

337 each data set A and B. In total, four 3D inversion models are presented here. Each

338 synthetic data set generated from models A and B were inverted using two different *a*

339 *priori* models: (1) a simple half-space of 100 Ω.m and (2) a 2D model closer to the

340 original 3D inversion models, with the aim of obtaining a more constrained inversion.

341 The resulting inversion models are identified as A1, A2, B1 and B2 (Fig. 5). In all

342 cases, the starting model used in the inversions was a uniform half-space of 100 Ω.m.

343 Similar to the real data inversion, here an error floor of 2.5% of the magnitude of the

344 geometrically-averaged off-diagonal impedances was used to set a minimum error bar

345 to $0.025 * (Z_{xy} * Z_{yx})^2$ applied on all four elements of the impedance tensor during the

346 inversion. Note that this is half the error floor defined for the real MT impedance data

347 (above).

348 First of all, both unconstrained models A1 and A2 show final overall RMS

349 misfits of 1.8. South of the profile the resistivity structure of the original models is

350 fairly well recovered, although the top of the conductive layer is seen at slightly

351 shallower depths. However, further north, where the environment becomes more 3D,

352 the lateral resolution of the intrusive structures becomes poorer as the mid-crustal

353 conductor dips steeply to the north. It is clear that for each model A1 and B1, the data

354 detect conductive structures due to the intrusions north of the profile. However, with

355 the poor lateral coverage related to the "one profile" configuration of the stations, the

356 conductive anomaly deepens to the north along the profile.

357   In order to compensate for the lack of lateral coverage, a second inversion

358 scheme was applied. Models A2 and B2 were obtained by introducing a new simple

359 2D *a priori* model closer to the original 3D synthetic models. This *a priori* model was

360 based particularly on the assumption of a horizontal conductive intrusion to the north

361 into a more resistive block (Fig. 5). For both inversions A2 and B2 the final overall

362 RMS misfit was reduced to 1.1 after following an identical inversion

363 parameterization as for models A1 and B1. Thus, the use of an *a priori* model has

364 allowed the inversion to avoid the local minimum associated with models A1 and B1

365 and to discover superior models that fit almost a factor of 2 better. It is worth noting

366 that the use of the new *a priori* model decreases also the individual RMS misfits for

367 all sites (Fig. 4). The main difference in the new A2 and B2 models is the substantial

368 improvement of the lateral resolution for the 3D intrusions located beneath the

369 northern part of the profile. Although, each intrusion obviously cannot be defined

370 clearly due to the 15 km width and depth of each anomaly, this second set of

371 inversions appears to be more sensitive to lateral structures. Even the preferential

372 orientation of the original intrusion can be recovered, as seen on model B2 where the

373 resistive and conductive anomalies are slightly orientated towards the east in the

374 northern part of the profile (Fig. 5). By forcing the embedding of the conductive layer

375 in the more resistive block, the conductive anomaly located previously deeper

376 beneath the profile is now relocated on each side of the profile, giving more support

377 to the original 3D models by improving lateral resolution somewhat.

378   Finally, in the northern part of the profile, the inversion can still sense the

379 resistor extending further with depth as in the original model, highlighting the

380 propagation of the sensitivity of the data beyond the constraints of the *a priori* model.

381 However, due to the sharp layer transition generated by the *a priori* model, inversions

382 could be inhibited and therefore must be viewed with caution. Figure 6 shows the

383   observed synthetic data generated from models A and B as well as the calculated MT

384   data from models A1, A2, B1 and B2. The main difference between the model A and

385   B can be clearly seen on the XX and YY components of the apparent resistivity. For

386   model A, the diagonal elements of the impedance tensor are quite low at all sites and

387   periods. Furthermore, although the effect of the introduction of the *a priori* model is

388   not obvious on the responses associated with model A, model B shows a net

389   improvement for the responses of the diagonal elements, particularly for apparent

390   resistivity.

391
392

393   ## 4.3.   **Constrained 3D inversion of the INDEPTH data**

394

395   Following the results of the synthetic study above, a second 3D inversion of

396   the INDEPTH data is presented here, where this time the inversion is controlled by

397   the use of a 2D *a priori* model. This *a priori* model was based on the previous MT

398   studies in the area (Unsworth et al., 2004; Le Pape et al., 2012) and is therefore very

399   similar to the 2D *a priori* model used in the above synthetic study. This new 3D

400   inversion followed a similar scheme to the first unconstrained model 1 presented

401   above (Fig. 3), with the only difference being the introduction of a different *a priori*

402   model. As seen on Figure 7, the inversion is controlled by a 2D model defined by a

403   30 Ω.m layer located between 20 and 70 km based on the assumption of whole

404   crustal partial melting. This layer is embedded in the more resistive block

405   characterizing the Kunlun-Qaidam terrane to the north. The latter is 600 Ω.m resistive

406   and limited to 100 km thickness extent in order to avoid too much of a resistive

407   constraint on the model. To the south, a 300 Ω.m layer describes the upper crust of

408   the Songpan-Ganzi terrane. Furthermore, the Qaidam basin was modelled by a 100

409   Ω.m 12 km thick layer to avoid the smearing of the highly conductive structure

410   characterizing the basin. The *a priori* model resistivities were chosen relatively close

411   to each other to limit significant lateral and vertical resistivity contrasts that could

412   lead to the generation of over-fitting artefacts in the model. Furthermore, the

413   transition between the two main blocks was located beneath the surficial trace of the

414   Kunlun fault.

415   The results of the inversion (Fig. 7) are interesting as they show an

416   improvement in fit to the data at some stations located north of the Kunlun fault and

417   contribute to an overall RMS misfit of 1.9. The observed and calculated MT data

418   obtained from model 2 is plotted on Figure 8. Furthermore, comparison of both

419   observed and calculated curves of apparent resistivity and phase for all 4 components

420   can be found in the supplementary information. The new restrictions applied to the

421   inversion through the use of 2D *a priori* model mainly enabled a limiting in the

422   downward leakage of some of the conductive artefacts observed in model 1 (Fig. 3).

423   In a similar manner to that demonstrated in the synthetic MT study, this new model

424   also improved the lateral resolution around the profiles. The plan view at 5 km depth

425   presents once again interesting correlations with the surficial traces of the major

426   tectonic features beyond the lateral boundaries created by the *a priori* model. To the

427   west, the SKF and KF describe the limit of the conductive sediments denoted by

428   feature "A" of the Songpan-Ganzi terrane. To the east, the upper crustal resistive

429   structures "C" can be related again to the Bayan Har mountains. The main resistive

430   features "B" observed on the models located north of the Kunlun fault likely define

431   extruded Proterozoic basement and plutonic intrusions characteristic of the Kunlun

432   Shan (Cowgill et al., 2003). The resistive structure located just south of the NKT at a

433   depth shallower than 30 km is likely to be part of the Kunlun Batholith, a significant

434   feature of the north Kunlun ranges (Yin and Harrison, 2000).

435   The extension of all different structures with depth can be seen on the cross-

436   sections 2 and 3 (Fig. 7). The horizontal slices at 20 km and 37 km particularly show

437   strong north-south aligned lateral changes in the resistivity structures. Those

438   alternations, more clearly seen in model 2 than in model 1, cross the Kunlun Fault to

439   the north. Indeed, beneath the Kunlun Fault system, the INDEPTH IV profile defines

440   a resistive feature surrounded by conductive material "F" on each of its sides. The

441 synthetic inversion study (Fig. 5) also confirms the fact that at middle-to-lower crust

442 depths the lateral resolution on structures at least 50 km outside the profiles is

443 reasonably accurate. Furthermore, as seen on model 1 another conductive anomaly

444 "E" is located between the KF and NKT, and seems to be superposed to the anomaly

445 intrusion from the south. This second conductive anomaly beneath the Kunlun Shan

446 could be linked to crustal fluids released from the southeast-dipping North Kunlun

447 Thrust. Cross-section 2 when compared to model 1 particularly highlights now the

448 clear intrusion of the conductive middle to lower crust "F" of the Songpan-Ganzi

449 terrane to the north across the Kunlun Fault. As mentioned previously, cross-section 1

450 is not well constrained and little can be concluded from it, but the aim here is to see

451 how the introduction of the resistive block removed the leakage of the conductivity

452 anomaly observed on the cross-section 1 of the model 1.

453

454

455 ## 5. Discussion and Interpretation

456

457 Although based on two MT profiles, and therefore characterized by

458 resolution issues associated with the paucity of spatial coverage, the 3D inversion

459 models reveal interesting features and show once again that the resistivity structure of

460 this part of the Tibetan plateau is spatially quite complex. The synthetic modelling

461 demonstrates that lateral resolution can be improved with the introduction of a trusted

462 *a priori* model. However, in order to constrain the full 3D structure, additional MT

463 profiles or a grid of MT stations are required to increase sensitivity and resolution,

464 both laterally and in depth (Siripunvaraporn et al., 2005b). In comparison to model 1,

465 some clear improvement in the lateral resolution of the 3D structures can be seen in

466 model 2. However, one comforting aspect in having the models 1 and 2 is the

467 consistency and reliability of some structures that are common features for both

468 models. Those are less likely to be artefacts of the inversion. Furthermore, as the *a*

469 *priori* model is an approximation, it may also control structures that are too confining,

470 and therefore the observations from the model 1 should not be neglected in the

471 interpretation.

472   Several interesting features can be seen in both models 1 and 2 and it is also

473 worth noting that the main observed conductive structures are quite in agreement with

474 the inductions arrows plotted on Figure 2. To the north, the geometry of the southern

475 part of the conductive Qaidam basin is well recovered spatially by the MT data and is

476 quite well constrained in the model 2. Furthermore, the high resistivity of the Kunlun-

477 Qaidam block, associated with its colder thermal conditions compared to the

478 Songpan-Ganzi block, is also a consistent feature from both inversions and extends to

479 depths of around 130 km, as seen on model 1. The later observation is in agreement

480 with the tomographic results from Ceylan et al. (2012). However, due to the lack of

481 stations, which inhibits resolution of mantle structures in the model, it is difficult to

482 exclude the model of Asian lithosphere subduction (Zhao et al., 2011).

483   Both models show also a conductive anomaly elongated along and located

484 south of the surficial trace of the North Kunlun thrust. This anomaly is elongated in

485 an east-west direction and propagates to the east with depth. One interpretation would

486 be the presence of fluids associated with the south-east dipping north Kunlun thrust.

487 To the south, both models 1 and 2 exhibit a widespread middle to lower crust

488 conductive anomaly extending to the South Kunlun Fault. Due to the presence of

489 strong crustal conductors and also the lack of lateral coverage, the resolution to the

490 mantle structures of the Songpan-Ganzi terrane is challenging. As discussed by Li et

491 al. (2003), it is possible that metallic minerals and graphite exists locally in Tibet.

492 However, since the main crustal anomaly beneath the Qiangtang and Songpan-Ganzi

493 terranes crosses major terrane boundaries as it extends further south in the Lhasa

494 terrane (Wei et al., 2001), graphite and metallic minerals are likely not responsible for

495 the observed large spatial extend of the crustal conductive anomaly. Furthermore,

496 Yoshino and Noritake (2011) have shown that graphite is not stable at the

497 temperatures expected to characterize the middle to lower Tibetan lower crust, i.e.,

498   temperatures in excess of 700°C.

499   The main crustal anomaly observed on the resistivity models has been
500   interpreted to be related to widespread partial melting of the middle-to-lower crust
501   (Unsworth et al., 2004; Le Pape et al., 2012). The partial melting of the crust under
502   anomalously high temperatures in the northern Tibetan (Owens and Zandt, 1997;
503   Mechie et al., 2004) is in agreement with the presence of thin Tibetan lithosphere
504   beneath northern Tibet (McNamara et al., 1997; Zhao et al., 2011; Agius and
505   Lebedev, 2013). The latter feature may enhance the heat flow in a crust already
506   exceptionally thick enough to produce high radiogenic heat generation. Furthermore,
507   the presence of partially molten crust is also in agreement with the presence of
508   Miocene to Quaternary felsic magmas in the southern Kunlun Shan, north of the
509   Kunlun fault. Those felsic magmas have been interpreted to originate from crustal
510   melts (Wang et al., 2012). Both models 1 and 2 show the intrusion of Songpan-Ganzi
511   conductive material to the north beyond the Kunlun Fault. Based on the assumption
512   that most of the conductive anomaly is associated with crustal melt, the constrained
513   3D model 2 presents superior resolution of the Songpan-Ganzi partially molten crust
514   melt intrusion to the north into the more resistive Kunlun-Qaidam block. Finally, it
515   can be noted that the evolution of the crustal conductive anomaly from south to north
516   is quite in agreement with the changes in the induction vectors orientations (Fig. 2).
517   South of the SKS, the vectors pointing to the south are quite strong and are associated
518   with a homogeneous conductive anomaly. North of the SKS, they become weaker
519   and west-oriented reflecting the lateral changes characterizing the conductive
520   intrusions observed in the 3D model.

521   These observations are very consistent with the results of 2D anisotropic
522   modelling of the 600-line (Le Pape et al., 2012). However, although the prior 2D
523   anisotropic study of Le Pape et al. (2012) mainly revealed the extension of the partial
524   melt from the Songpan-Ganzi crust further north in a finger-like manner of intrusion,
525   the results drawn from the modelling did not bring further constraints on the

geometry of the observed anomaly. The new models and results associated with the introduction of the new INDEPTH IV MT data bring a superior understanding on the distribution of those intrusions. The 3D model 2 particularly highlights not only one but two north-south orientated intrusive channels located on each side of the INDEPTH IV profile. Despite resolution issues at the depth of the anomaly, the electrical anisotropy previously observed in the area appears to be more likely related to macroscopic anisotropy associated with a heterogeneous extension of the partial molten Songpan-Ganzi crust to the north. The locations of the two INDEPTH profiles particularly enable us to constrain an upper limit on the width of one of the channels. Indeed, the conductive anomaly located between the two profiles and extending across the Kunlun fault appears to be 40 to 50 km wide as it is surrounded by trusted and well resolved lateral resistive features.

Despite a better understanding in the geometry of the intrusive anomaly, as seen on the synthetic modelling (Fig. 5), the 3D inversion of the profile data struggles to recover the true resistivity of the original anomaly, particularly for structures off-profile. Therefore, at this stage only approximate estimates of the fraction of melts have been considered. The more conductive anomaly "E" (Fig. 7) located just south of the NKT was not taken into account as probably it is involving crustal fluids released from the NKT. Based on the 3D model 2, the Sonpan-Ganzi crust high conductivity anomaly is mainly ranging between 3 to 10 Ω.m in resistivity, whereas for the Kunlun crust the resistivity of the anomaly ranges from 6 to 30 Ω.m. Using the Partzsch et al. (2000) modified brick layer model, the fraction of melt beneath the Songpan-Ganzi terrane is expected to be between 4% and 15%, in agreement with previous studies (Bai et al., 2010; Rippe and Unsworth, 2010), whereas for the Kunlun crust the intrusive channels would have lower fractions of melt ranging from 2% to 8%. Following the arguments of Rippe and Unsworth (2010), it is concluded that the decrease of melt fraction to the north implies a reduction of viscosity and therefore a decrease in the velocity of flow along the channels. Furthermore, with a

limited signature of channel flow at the surface, the separated intrusive channels of the Songpan-Ganzi crust are probably flowing in a similar manner as the "tunnel flow model" presented by Beaumont et al. (2001). Finally, the overall viscosity of the Kunlun crust would still be in agreement with a significant drop in viscosity as observed by Ryder et al. (2011), reflecting the lateral changes in the rheology of the Kunlun crust emphasised by the 3D resistivity modelling.

6. Acknowledgements

7. References

Agius, M.R., Lebedev, S., 2013. Tibetan and Indian lithospheres in the upper mantle beneath Tibet: Evidence from broadband surface-wave dispersion. Accepted in Geochemistry, Geophysics, Geosystems.

Bai, D., Unsworth, M.J., Meju, M.A., Ma, X., Teng, J., Kong, X., Sun, Y., Sun, J., Wang, L., Jiang, C., Zhao, C., Xiao, P., Liu, M., 2010. Crustal deformation of the eastern Tibetan plateau revealed by magnetotelluric imaging. Nature Geoscience 3, 358-362.

585 Beaumont, C., Jamieson, R.A., Nguyen, M.H., Lee, B., 2001. Himalayan tectonics
586   explained by extrusion of a low-viscosity channel coupled to focused surface
587   denudation. Nature 414, 738–742.

588 Burchfiel, B.C., Chen, Z., Liu, Y., Royden, L.H., 1995. Tectonics of the Longmen
589   Shan and adjacent regions, central China. Int. Geol. Rev. 37, 661–735.

590 Caldwell, T.G., Bibby, H.M., Brown, C., 2004. The magnetotelluric phase tensor.
591   Geophys. J. Int. 158, 457–469.

592 Ceylan, S., Ni, J., Chen, J.Y., Zhang, Q., Tilmann, F., Sandvol, E., 2012. Fragmented
593   indian plate and vertically coherent deformation beneath eastern Tibet. J.
594   Geophys. Res. 117, B11303.

595 Chen, L.H., Booker, J.R., Jones, A.G., Wu, N., Unsworth, M.J., Wei, W.B., Tan,
596   H.D. 1996. Electrically conductive crust in southern Tibet from INDEPTH
597   magnetotelluric surveying. Science, 274, 1694-1696.

598 Clark, M.K., Royden, L.H., 2000. Topographic ooze: Building the eastern margin of
599   Tibet by lower crustal flow. Geology 28, 703–706.

600 Cowgill, E., Yin, A., Harrison, T.M., Xiao-Feng, W., 2003. Reconstruction of the
601   Altyn Tagh fault based on U-Pb geochronology: Role of back thrusts, mantle
602   sutures, and heterogeneous crustal strength in forming the Tibetan Plateau. J.
603   Geophys. Res. 108(B7), 2346.

604 Egbert, G.D., 1997. Robust multiple-station magnetotelluric data processing.
605   Geophys. J. Int. 130, 475–496.

606 Gehrels, G.E., Kapp, P., DeCelles, P., Pullen, A., Blakey, R., Weislogel, A., Ding, L.,
607   Guynn, J., Martin, A., McQuarrie, N., Yin, A., 2011. Detrital zircon
608   geochronology of pre-Tertiary strata in the Tibetan-Himalayan orogen.
609   Tectonics 30, TC5016.

610 Godin, D., D. Grujic, R. D. Law, and M. P. Searle, Channel Flow, Ductile Extrusion
611   and Exhumation in Continental Collision Zones, vol. 268, chap. Channel flow,
612   ductile extrusion and exhumation in continental collision zones: an

introduction, pp. 1–23, R. D. Law, M. P. Searle and L. Godin ed., Geological Society, London, Special Publications,2006.

Haines, S.S., Klemperer, S.L., Brown, L., Jingru, G., Mechie, J., Meissner, R., Ross, A., Wenjin, Z., 2003. INDEPTH III seismic data: From surface observations to deep crustal processes in Tibet. Tectonics 22.

Harris, N., Channel flow and the Himalayan-Tibetan orogen: a critical review, Journal of the Geological Society, *164*(*3*), 511–523, 2007.

Huang, C.K., Ye, T.Z., Chen, K.Q., Wu, K.L., Ji, X.Y., Gao, Z.J., Qian, D.D., Tian, Y.Y., He, Y.X., Zhan, Q.H., Cao, B.G., Li, L., Shao, H.M., Wang, Y.Q., Yang, M.G., Zhang, Z.W., Yao, D.S., Zheng, J.K., 2004. Geological Map of the People's Republic of China. SinoMaps Press, Xian.

Jones, A.G. 1986. Parkinson's pointers' potential perfidy! Geophysical Journal of the Royal Astronomical Society, 87, 1215-1224.

Jones, A.G. 2012. Distortion of magnetotelluric data: its identification and removal, In "The Magnetotelluric Method: Theory and Practice", Chapter 6, eds. A.D. Chave and A.G. Jones. Cambridge University Press, Cambridge (UK).

Jones, A.G., Chave, A.D., Egbert, G.D., Auld, D., Bahr, K., 1989. A comparison of techniques for magnetotelluric response function estimates. J. Geophys. Res. 94, 14,201–14,213.

Jones, A.G., Jödicke, H., 1984. Magnetotelluric transfer function estimation improvement by a coherence-based rejection technique. 54th Ann. Mtg. Soc. of Expl. Geophys., Atlanta, Georgia .

Karplus, M.S., Klemperer, S.L., Lawrence, J.F., Zhao, W., Mechie, J., Tilmann, F., Sandvol, E., Ni, J., 2013. Ambient-noise tomography of north tibet limits geological terrane signature to upper-middle crust. Geophysical Research Letters 40, 808–813.

Karplus, M.S., Zhao, W., Klemperer, S.L., Wu, Z., Mechie, J., Shi, D., Brown, L.D., Chen, C., 2011. Injection of Tibetan crust beneath the south Qaidam Basin:

641 Evidence from INDEPTH IV wide-angle seismic data. J. Geophys. Res. 116.

642 Kezao, C., Bowler, J.M., 1986. Late pleistocene evolution of salt lakes in the Qaidam
643 basin, Qinghai province, China. Palaeogeography, Palaeoclima- tology,
644 Palaeoecology 54.

645 Kirby, E., Harkins, N., Wang, E., Shi, X., Fan, C., Burbank, D., 2007. Slip rate
646 gradients along the eastern Kunlun fault. Tectonics 26.

647 Kiyan, D., Jones, A.G., Vozar, J., 2013. The inability of magnetotelluric off-diagonal
648 impedance tensor elements to sense oblique conductors in 3d inversion.
649 Accepted in Geophysical Journal International .

650 Klemperer, S., 2006. Channel Flow, Ductile extrusion and exhumation in
651 Continental Collision Zones. R. D. Law, M. P. Searle and L. Godin ed.
652 Geological Society, London, Special Publications, volume 268, chapter Crustal
653 flow in Tibet: Geophysical evidence for the physical state of Tibetan
654 lithosphere, and inferred patterns of active flow, pp. 39–70.

655 Le Pape, F., Jones, A.G., Vozar, J., Wenbo, W., 2012. Penetration of crustal melt
656 beyond the Kunlun fault into northern Tibet. Nature Geoscience 5, 330–335.

657 Li, S., Unsworth, M.J., Booker, J.R., Wei, W., Tan, H., Jones, A.G., 2003. Partial
658 melt or aqueous fluids in the Tibetan crust: Constraints from INDEPTH
659 magnetotelluric data. Geophys. J. Int. 153, 289–304.

660 Mackie, R.L., Smith, J.T., Madden, T.R., 1994. Three-dimensional electro- magnetic
661 modeling using finite difference equations: the magnetotelluric example. Radio
662 Sci. 29, 923–935.

663 McNamara, D.E., Walter, W.R., Owens, T.J., Ammon, C.J., 1997. Upper mantle
664 velocity structure beneath the Tibetan Plateau from pn travel time tomography.
665 J. Geophys. Res. 102(B1), 493–505.

666 Mechie, J., Sobolev, S.V., Ratschbacher, L., Babeyko, A.Y., Bock, G., Jones, A.G.,
667 Nelson, K.D., Solon, K.D., Brown, L.D., Zhao, W., 2004. Precise temperature
668 estimation in the tibetan crust from seismic detection of the α-β quartz

669   transition. Geology 32, 601–604.

670 Mechie, J., Zhao, W., Karplus, M.S., Wu, Z., Meissner, R., Shi, D., Kemplerer, S.L.,
671   H[]Su, Kind, R., Xue, G., Brown, L.D., 2012. Crustal shear velocity and
672   Poisson's ratio structure along the INDEPTH IV profile in northeast Tibet as
673   derived from wide-angle seismic data. Geophys. J. Int. 191, 369–384.

674 Medvedev, S., Beaumont, C., 2006. Channel Flow, Ductile Extrusion and
675   Exhumation in Continental Collision Zones. R. D. Law, M. P. Searle and L.
676   Godin ed.. Geological Society, London, Special Publications. Volume 268.
677   chapter Growth of continental plateaus by channel injection: models designed
678   to address constraints and thermomechanical consistency. pp. 147–164.

679 Meyer, B., Tapponnier, P., Bourjot, L., Metivier, F., Gaudemer, Y., Peltzer, G.,
680   Shunmin, G., Zhitai, C., 1998. Crustal thickening in Gansu Qinghai,
681   lithospheric mantle subduction, and oblique, strike slip controlled growth of the
682   Tibet plateau. Geophysical Journal International 135(1), 1–47.

683 Nelson, K.D., Zhao, W., Brown, L.D., Kuo, J., Che, J., Liu, X., Klemperer, S.L.,
684   Makovsky, Y., Meissner, R., Mechie, J., Kind, R., Wenzel, F., Ni, J.,
685   Nabelek, J., Chen, L., Tan, H., Wei, W., Jones, A.G., Booker, J.,
686   Unsworth, M., Kidd, W.S.F., Hauck, M., Alsdorf, D., Ross, A., Cogan, M.,
687   Wu, C., Sandvol, E., Edwards, M., 1996. Partially molten middle crust
688   beneath southern Tibet: Synthesis of Project INDEPTH results. Science 274,
689   1684–1686.

690 Owens, T.J., Zandt, G., 1997. Implications of crustal property variations for models
691   of Tibetan plateau evolution. Nature 387, 37–43.

692 Parkinson, W.D., 1959. Directions of rapid geomagnetic fluctuations. Geo- physical
693   Journal of the Royal Astronomical Society 2(1), 1–14.

694 Partzsch, G. M., F. R. Schilling, and J. Arndt, The influence of partial melting on the
695   electrical behavior of crustal rocks: laboratory examinations, model calculations
696   and geological interpretations, Tectonophysics, *317*, 189–203, 2000.

697 Rippe, D., Unsworth, M., 2010. Quantifying crustal flow in Tibet with mag-
698   netotelluric data. Physics of the Earth and Planetary Interiors 179, 107– 121.

699 Rousseeuw, P.J. 1984. Least median of squares regression. Journal of the American
700   Statistical Association, 79, 871-880.

701 Royden, L.H., Burchfiel, B.C., King, R.W., Wang, E., Chen, Z., Shen, F., Liu, Y.,
702   1997. Surface deformation and lower crustal flow in eastern Tibet. Science
703   276, 788–790.

704 Searle, M. P., J. R. Elliott, R. J. Phillips, and S. L. Chung, Crustal-lithospheric
705   structure and continental extrusion of Tibet, Journal of the Geological Society,
706   London, *168*, 633–672, 2011.

707 Siripunvaraporn, W., Egbert, G., Lenbury, Y., Uyeshima, M., 2005a. Three-
708   dimensional magnetotelluric inversion: data-space method. Physics of the
709   Earth and Planetary Interiors 150, 3–14.

710 Siripunvaraporn, W., Egbert, G., Uyeshima, M., 2005b. Interpretation of two-
711   dimensional magnetotelluric profile data with three-dimensional inversion:
712   synthetic examples. Geophys. J. Int. 160, 804–814.

713 Smirnov, M.Y., 2003. Magnetotelluric data processing with a robust statistical
714   procedure having a high breakdown point. Geophysical Journal International
715   152, 1–7.

716 Tapponnier, P., Xu Zhiqin, X., Roger, F., Meyer, B., Arnaud, N., Wittlinger G.,
717   Jingsui Y., (2001), Oblique stepwise rise and growth of the Tibet Plateau,
718   Science, 294, 1671 –1677.

719 Unsworth, M., Wei, W., Jones, A.G., Li, S., Bedrosian, P., Booker, J., Jin, S., Deng,
720   M., Tan, H., 2004. Crustal and upper mantle structure of northern Tibet imaged
721   with magnetotelluric data. J. Geophys. Res. 109, B02403.

722 Wang, Q., Chung, S.L., Li, X.H., Wyman, D., Li, Z.X., Sun, W.D., Qiu, H.N., Liu,
723   Y.S., Zhu, Y.T., 2012. Crustal Melting and Flow beneath Northern Tibet:
724   Evidence from Mid-Miocene to Quaternary Strongly Peraluminous Rhyolites in

725   the Southern Kunlun Range. Journal of Petrology 53 (12), 2523-2566.

726   Wei, W., Unsworth, M., Jones, A.G., Booker, J., Tan, H., Nelson, D., Chen, L., Li, S.,

727   Solon, K., Bedrosian, P., Jin, S., Deng, M., Ledo, J., Kay, D., Roberts, B., 2001.

728   Detection of widespread fluids in the Tibetan crust by magnetotelluric studies.

729   Science 292, 716–718.

730   Yao, H.J., Beghein, C., Van Der Hilst, R.D., 2008. Surface wave array tomography in

731   SE Tibet from ambient seismic noise and two-station analysis-II. Crustal and

732   upper-mantle structure. Geophysical Journal International 173, 205–219.

733   Yin, A., Chen, X., McRivette, M.W., Wang, L., Jiang, W., 2008. Cenozoic tectonic

734   evolution of qaidam basin and its surrounding regions (part 1): The north

735   qaidam thrust system. Geological Society of America Bulletin 120, 813–846.

736   Yin, A., Harrison, T.M., 2000. Geologic Evolution of the Himalayan-Tibetan Orogen.

737   Annual Review of Earth and Planetary Sciences 28(1), 211–280.

738   Yin, A., Nie, S., 1996. A phanerozoic palinspastic reconstruction of China and its

739   neighboring regions. In The Tectonics of Asia, ed. A. Yin, T.M. Harrison, New

740   York: Cambridge Univ. Press , 442–485.

741   Yoshino, T., Noritake, F., 2011. Unstable graphite films on grain boundaries in

742   crustal rocks. Earth and Planetary Science Letters, 306, 186-192.

743   Zhao, W., Kumar, P., Mechie, J., Kind, R., Meissner, R., Wu, Z., Shi, D., Su, H.,

744   Xue, G., Karplus, M., Tilmann, F., 2011. Tibetan plate overriding the Asian

745   plate in central and northern Tibet. Nature Geosci. 4, 870–873.

Figures

Figure 1: Sites location for the MT data used in the 3D inversion. The data used combine selected sites from both INDEPTH III (black) and IV (purple) profiles. ATF, Altyn Tagh Fault; KF, Kunlun Fault; MBT, Main boundary thrust; JRS, Jinsha River Suture; SKF, South Kunlun Fault; NKT, North Kunlun Thrust.
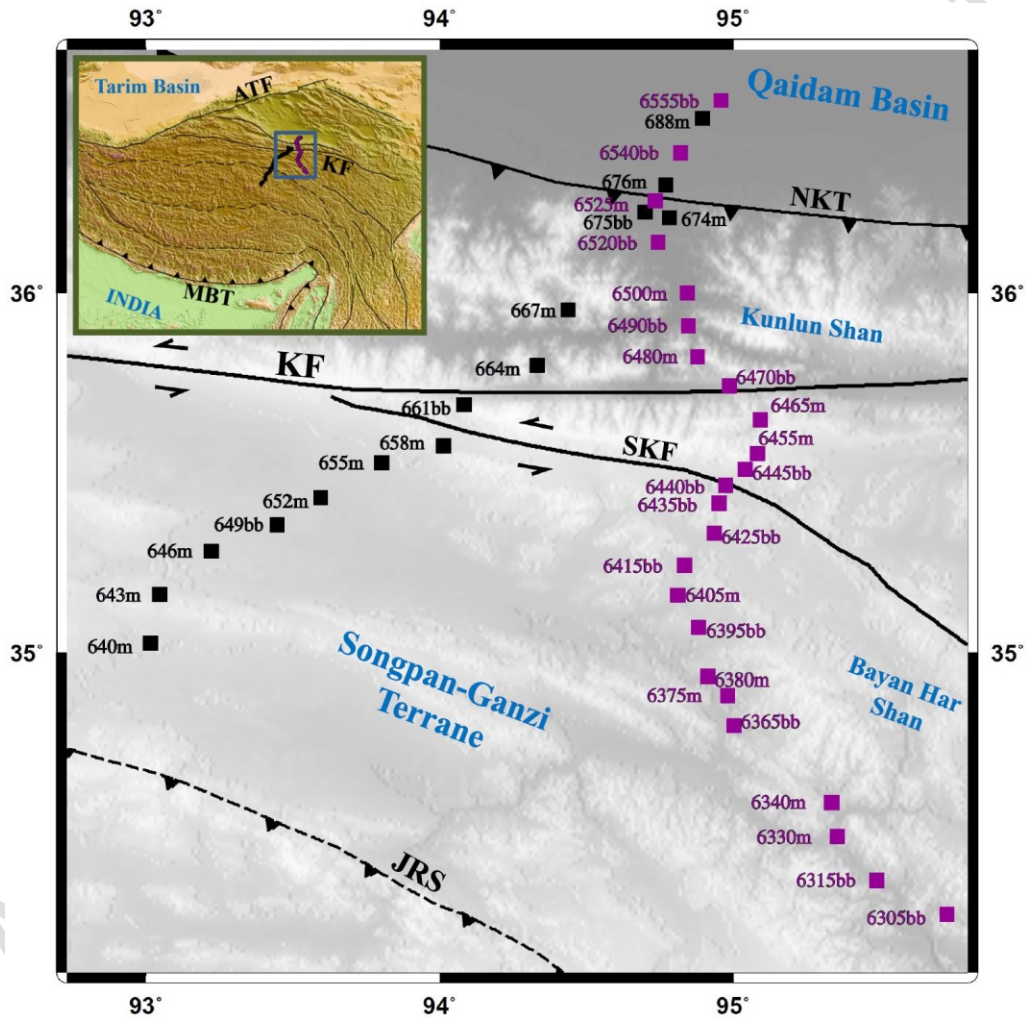
Figure 2: Induction arrows (only selected sites) and Phase tensor ellipses for the INDEPTH sites plotted for different period intervals. The real induction arrows are plotted under Parkinson's convention. For the induction vectors' errors, the errors are plotted as ellipses that indicate the deviation from each component of the induction vector. The ellipses are normalized by their major axes and filled with the *skew angle*. The ellipses are plotted so that the horizontal axis corresponds to an east-west orientation. The errors on the skew angle are plotted on top of each phase tensor ellipses.
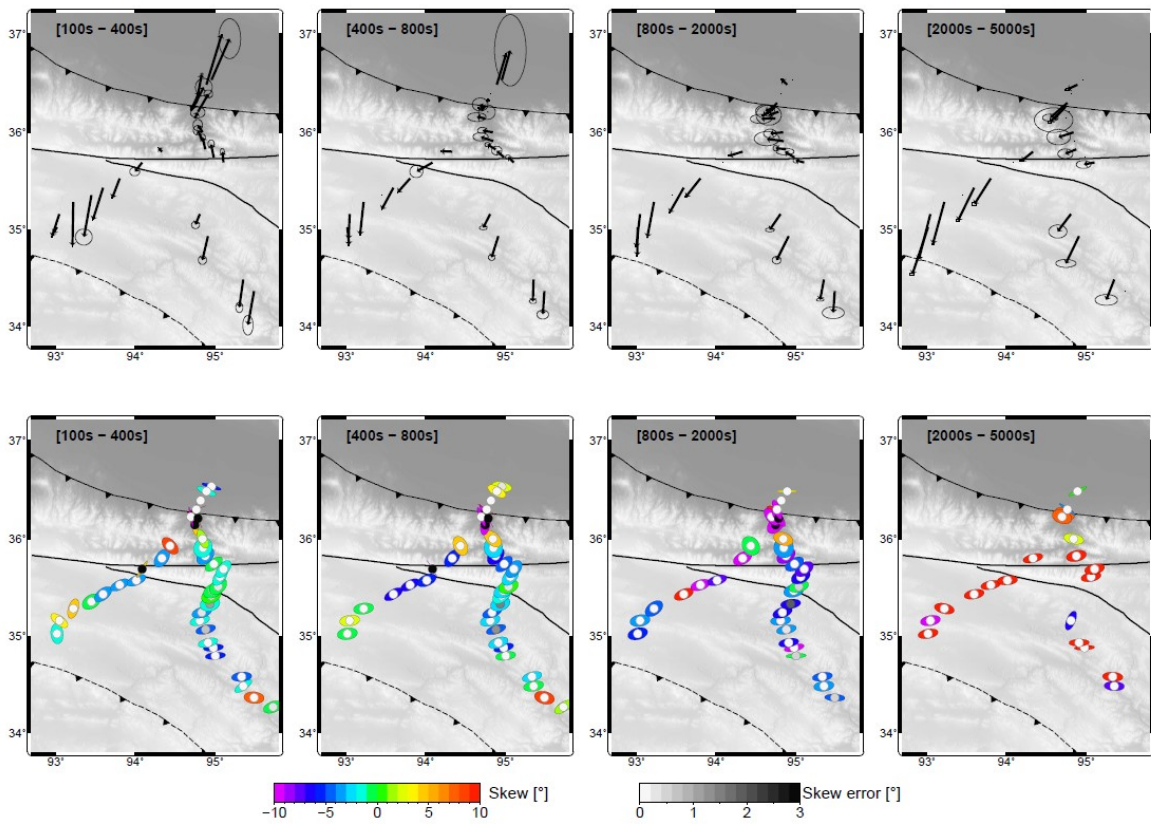
Figure 3: 3D model 1 of the INDEPTH data obtained from the inversion of the full impedance tensor. The 3D model is plotted for several horizontal slices at different depths and for cross-sections with locations shown on plane views. The RMS misfit of the inversion is shown for each site on the top right corner. KF, Kunlun Fault; SKF, South Kunlun Fault; NKT, North Kunlun Thrust.
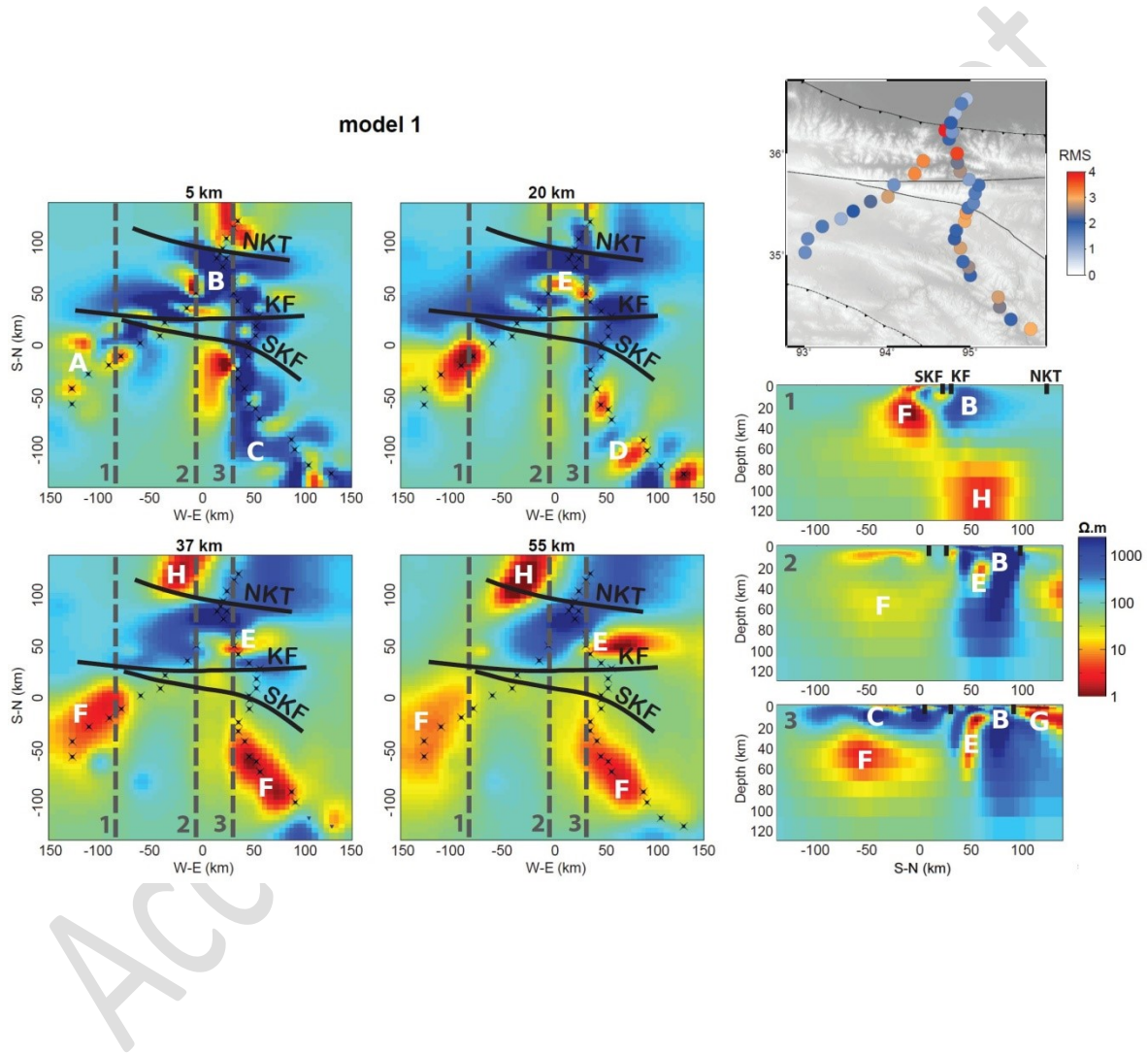
<u>Figure 4:</u> Observed and calculated data from the inversion model 1. The data is separated as INDEPTH III and IV sections. For each section, the station numbers increase to the north. The data is plotted as pseudo-sections of apparent resistivity and phase for all 4 components of the impedance tensor.
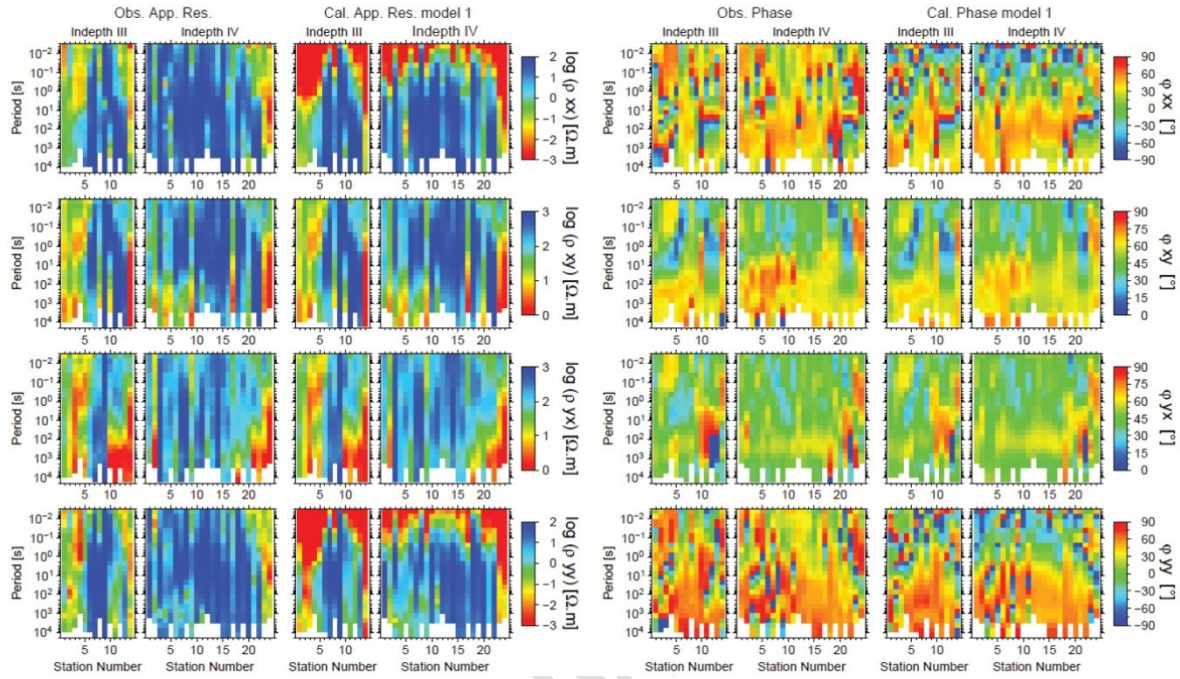
Figure 5: 3D synthetic study - The 3D synthetic models consist on a 1500 Ω.m resistive and 150 km thick block to the north. The southern block is 500 Ω.m resistive and 70 km thick with an embedded 2 Ω.m conductive layer between 30 and 50 km. The later turns into 3D intrusions in the more resistive block: the only difference between models A and B. Both blocks are underlain by a 100 Ω.m half-space. The inversion results for inversions A1, A2, B1 and B2 are presented with a plane view at 30 km as well as north- south cross-sections right beneath the stations. The RMS misfit is plotted for each site for each inversion. For inversion 2, the *a priori* model is mainly defined by relatively thicker 30 Ω.m m30id-lower crustal layer embedded into a thinner 600 Ω.*m* resistive block to the north and overlain by a 300 Ω.*m* layer to the south.
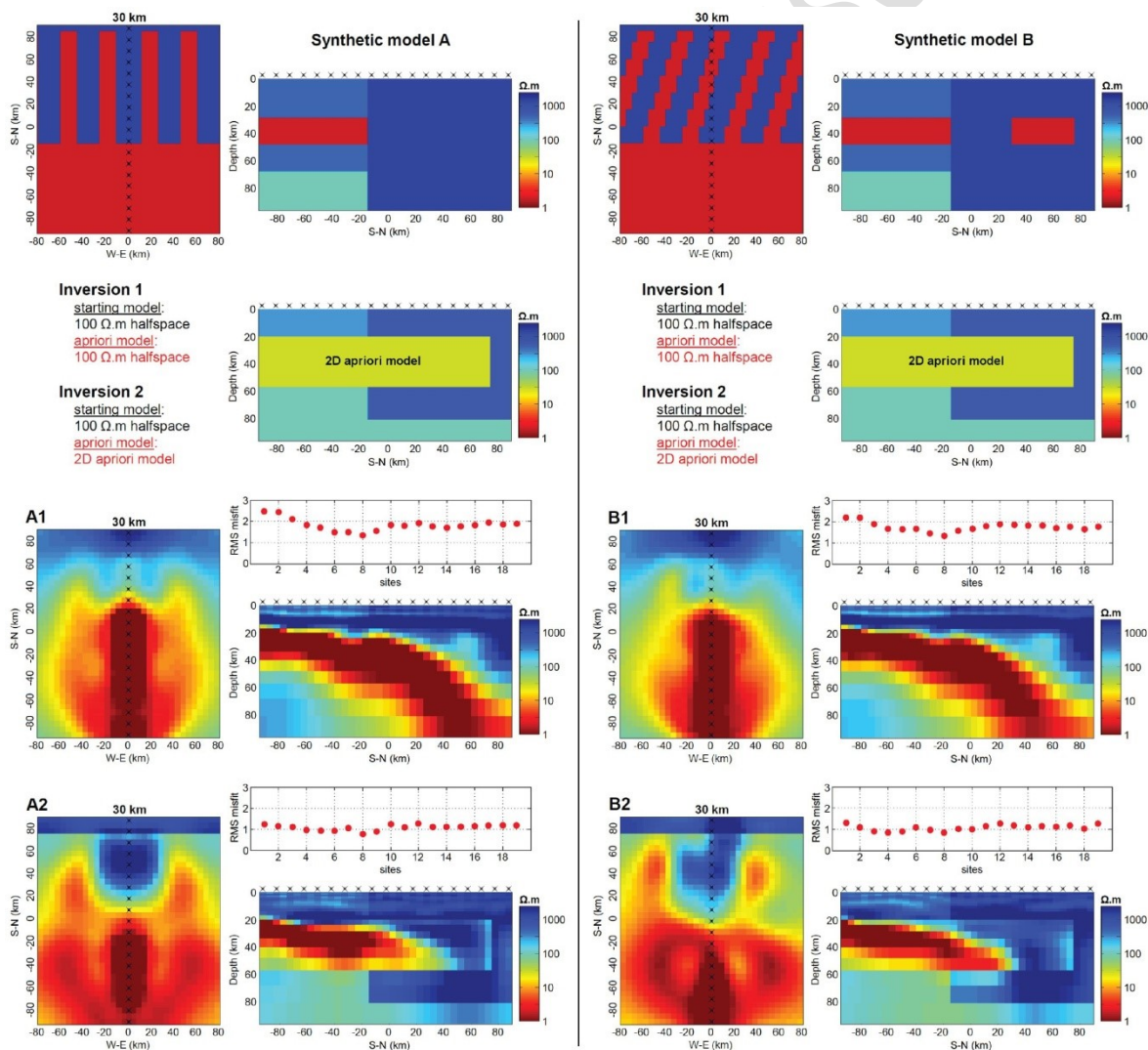
Figure 6: Observed synthetic data generated from models A and B associated with calculated data from the inversion models A1, A2, B1 and B2. The station numbers increases to the north. The data is plotted as pseudo-sections of apparent resistivity and phase for all 4 components of the impedance tensor.
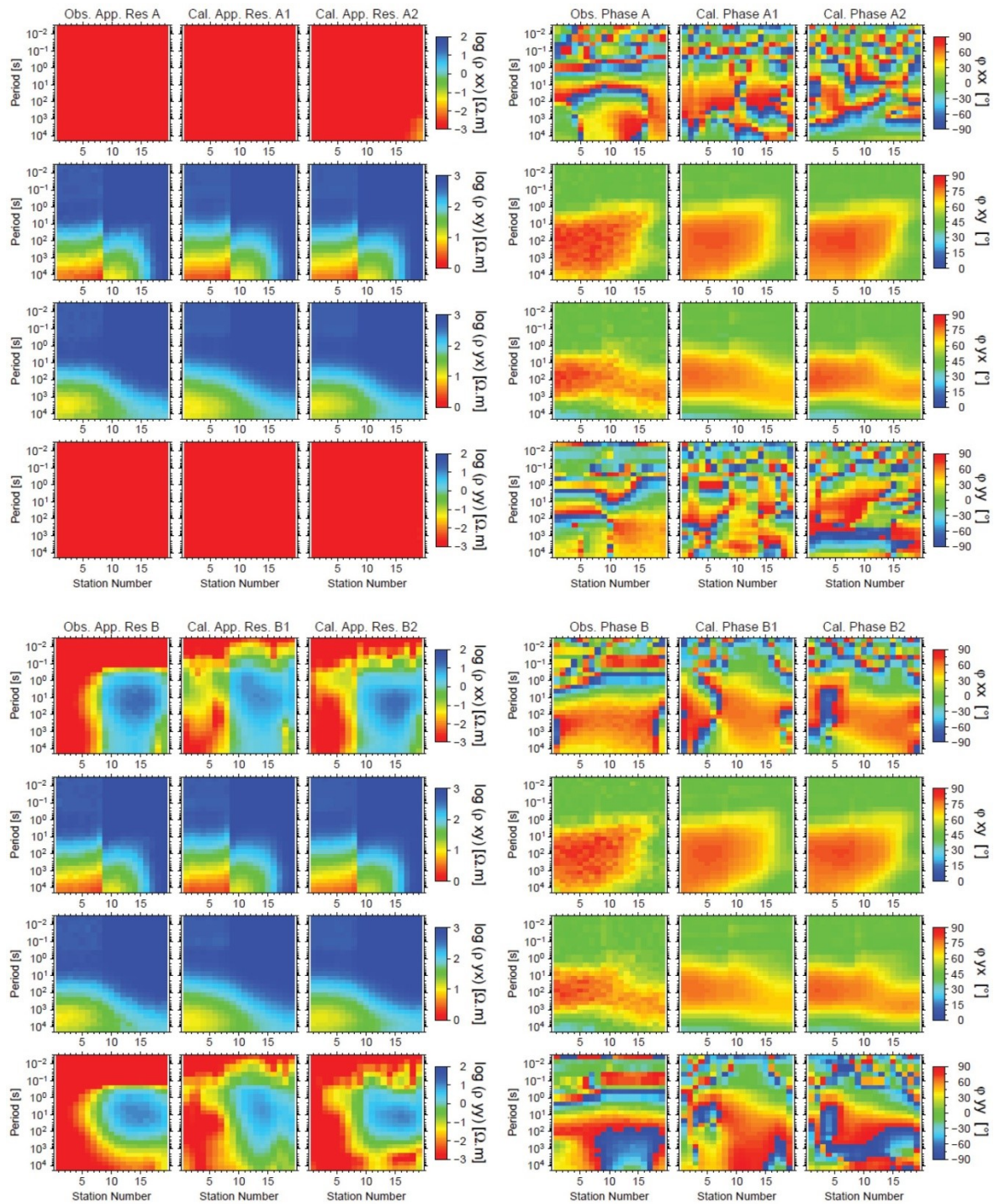
Figure 7: 3D model 2 of the INDEPTH data obtained from the inversion of the full impedance tensor and constrained by a 2D a priori model. The 3D model is plotted for several horizontal slices at different depths and for cross-sections with locations shown on plane views. The RMS misfit of the inversion is shown for each site on the top right corner. KF, Kunlun Fault; SKF, South Kunlun Fault; NKT, North Kunlun Thrust.
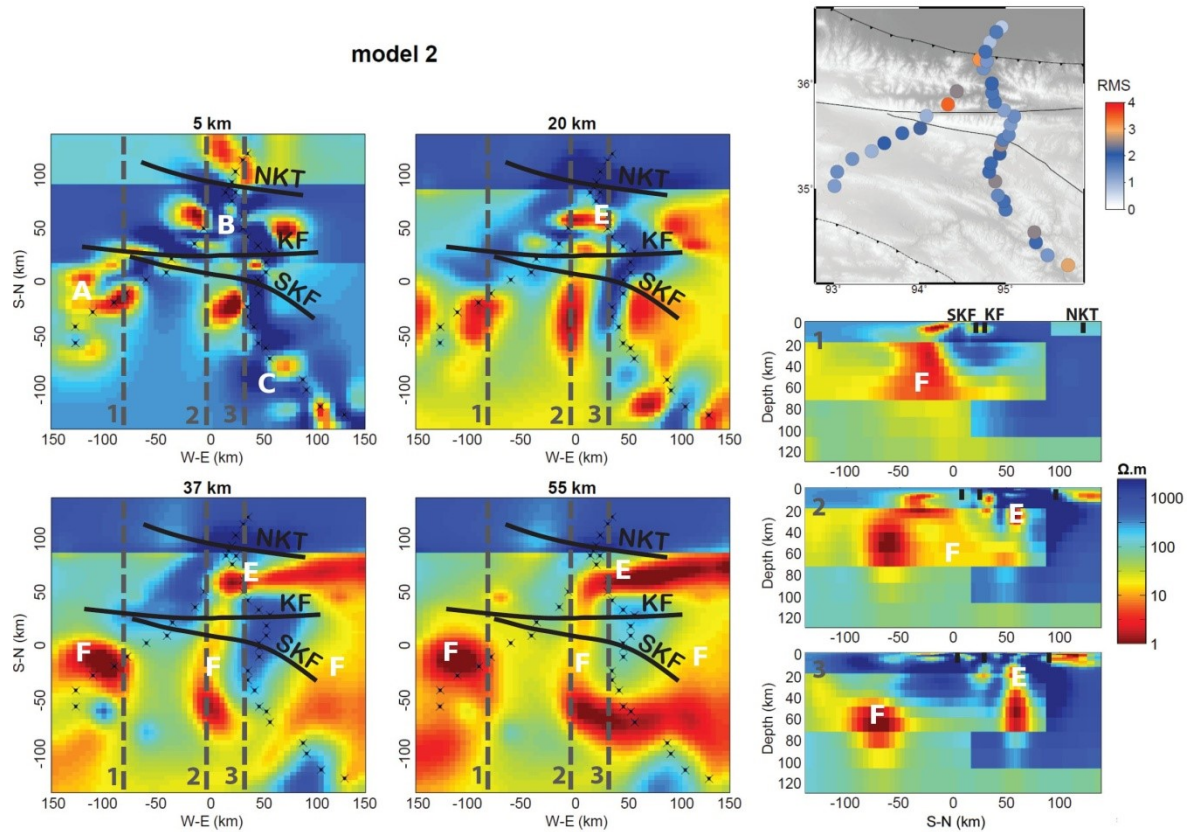
Figure 8: Observed and calculated data from the inversion model 2. The data is separated as INDEPTH III and IV sections. For each section, the station numbers increase to the north. The data is plotted as pseudo-sections of apparent resistivity and phase for all 4 components of the impedance tensor.